





Vertical Shear Instability in Thermally-Stratified Protoplanetary Disks: II. Hydrodynamic Simulations and Observability

HAN-GYEOL YUN ^{1,2} WOONG-TAE KIM ^{1,2} JAEHAN BAE ³ AND CHEONGHO HAN ⁴

¹*Department of Physics & Astronomy, Seoul National University, Seoul 08826, Korea*

²*SNU Astronomy Research Center, Seoul National University, 1 Gwanak-ro, Gwanak-gu, Seoul 08826, Republic of Korea*

³*Department of Astronomy, University of Florida, Gainesville, FL 32611, USA*

⁴*Department of Physics, Chungbuk National University, Cheongju 28644, Republic of Korea*

(Received XXX; Revised XXX; Accepted XXX)

ABSTRACT

We conduct three-dimensional hydrodynamic simulations to investigate the nonlinear outcomes and observability of vertical shear instability (VSI) in protoplanetary disks. Our models include both vertically isothermal and thermally stratified disks, with the latter representing realistic conditions featuring a hotter atmosphere above the midplane. We find that the VSI grows more rapidly and becomes stronger in thermally stratified disks due to enhanced shear, resulting in higher levels of turbulence. At saturation, the turbulence stress reaches $\alpha_{R\phi} \gtrsim 10^{-3}$, more than an order of magnitude stronger than the isothermal case. The saturated turbulence is more pronounced near the disk surfaces than at the midplane. On synthetic velocity residual maps, obtained by subtracting the Keplerian rotational velocity, perturbations driven by the VSI manifest as axisymmetric rings in isothermal disks and as ring segments in thermally stratified disks. The latter are visible at disk inclinations as high as 45° in thermally stratified disks. The amplitudes of these residual velocities range from ~ 50 to $\sim 100 \text{ m s}^{-1}$ at a 20° inclination, with larger values corresponding to greater thermal stratification. The magnitude of the observed velocity residual increases with the optical depth of the tracer used, as optically thick lines probe the regions near the disk surfaces.

Keywords: Protoplanetary disks (1300), Hydrodynamical simulations (767), Hydrodynamics (1963), Radiative transfer (1335), Accretion (14)

1. INTRODUCTION

Gas in a protoplanetary disk (PPD) gradually moves radially inward while following nearly Keplerian rotation around a central star. Shakura & Sunyaev (1973) and Lynden-Bell & Pringle (1974) attributed mass accretion to turbulent viscosity, which transports angular momentum radially outward. Since then, numerous studies have investigated the mechanisms that generate turbulence within PPDs (see Lesur et al. 2023 and references therein). In hot accretion disks surrounding compact objects, the magnetorotational instability (MRI) identified by Balbus & Hawley (1991) has long been considered the most promising source of turbulence. Due

to self-shielding, however, the majority of gas in PPDs has a low ionization fraction and temperature, which suppresses MRI activity except in the surface layers. Various non-ideal magnetohydrodynamic (MHD) simulations have supported the notion of inefficient MRI in driving turbulence in PPDs (Bai & Stone 2013; Simon et al. 2013; Lesur et al. 2014). This raises the question of what mechanisms drive turbulence and mass accretion in these disks.

The vertical shear instability (VSI) is a potential mechanism for turbulence driving within a PPD. Its operation requires a vertical variation of rotational angular velocity, which is readily achieved in PPDs due to the decreasing gravitational influence of the central star with increasing height and the decreasing disk temperature with radius (Urpin & Brandenburg 1998; Nelson et al. 2013). Although originally proposed for an-

gular momentum transport in the radiative zone of a differentially rotating star (Goldreich & Schubert 1967; Fricke 1968), the VSI has gained attention in the context of accretion disks following various analytical (Urpin & Brandenburg 1998; Urpin 2003) and numerical studies (Nelson et al. 2013; Stoll & Kley 2014). Since the VSI is purely a hydrodynamical process, it can operate even in cold regions where MRI is suppressed.

Previous numerical studies have revealed various characteristics of the VSI, including the meridional circulation pattern of its perturbation, which exhibit a radially narrow and vertically elongated structure (Nelson et al. 2013; Stoll & Kley 2014). This results in anisotropic turbulence with stronger vertical motion compared to radial motion (Stoll et al. 2017). Additionally, it has been shown that the VSI can persist despite stabilization by vertical buoyancy and magnetic fields (Nelson et al. 2013; Latter & Papaloizou 2018), as well as through radiative diffusion, (Stoll & Kley 2014) and non-ideal MHD effects (Cui & Bai 2020).

While the theoretical and numerical studies mentioned above suggest the PPDs are likely turbulent presumably due to the VSI, observational confirmations have been lacking. Recent advancements in spectral and spatial resolution, as well as sensitivity, have made it possible to measure turbulence levels in PPDs (Flaherty et al. 2015; Teague et al. 2016; see reviews by Rosotti 2023). Direct measurements of molecular line broadenings in sub-millimeter wavelengths suggest that turbulence in PPDs is at the level of $\delta v_{\text{turb}} \lesssim 10^{-1} c_s$, with c_s being the isothermal speed of sound, in disks around HD163296, TW Hya, MWC 380 and V4046 Sgr (Flaherty et al. 2015, 2017, 2018, 2020; Teague et al. 2018). Indirect measurements based on dust diffusion (Dullemond et al. 2018; Facchini et al. 2020; Rosotti et al. 2020), disk size (Trapman et al. 2020), and accretion rate (Rosotti et al. 2019) also indicate similar upper limits for turbulence levels in the disks. These levels are overall comparable to $\delta v_{\text{turb}} \sim 0.05 c_s$ predicted by numerical simulations of VSI in PPDs (Flock et al. 2017, 2020).

Recent observational techniques also now enable the probing of the dynamical structure of disks and the detection of small velocity perturbations on the order of $\sim 10 \text{ m s}^{-1}$ (Teague et al. 2021). This advancement opens up the possibility of detecting anisotropic turbulent motions in PPDs using molecular lines with Atacama Large Millimeter/submillimeter Array (ALMA). Barraza-Alfaro et al. (2021) recently reported that turbulent motions induced by the VSI are significant enough to be detectable with ALMA, appearing as various quasi-axisymmetric rings in velocity residual maps derived from molecular line emission images.

While the numerical models of Barraza-Alfaro et al. (2021) suggest that VSI-driven turbulence may possess observable signatures, they were restricted to vertically isothermal disks. However, real disks naturally exhibit thermal stratification caused by irradiation from the central star, which heats the surfaces preferentially, leaving optically thick regions near the midplane (see, e.g., Chiang & Goldreich 1997; D’Alessio et al. 1998, 1999). As the vertical profile of the rotational velocity is influenced by the pressure gradient, the characteristics of the VSI in thermally stratified disks are anticipated to differ from those in isothermal counterparts.

In our previous work, Yun et al. (2024, hereafter Paper I), we examined the linear stability of the VSI in thermally stratified disks using both local and semi-global approaches. Our analysis revealed that the VSI manifests in two distinct modes: surface and body modes (see also Nelson et al. 2013; Barker & Latter 2015). Surface modes localize in regions with strong shear, while body modes are distributed throughout the main body of a disk. In thermally stratified disks, surface modes bifurcate into two branches. The branch associated with the strongest shear at mid-height regions exhibits higher growth rates compared to the other branch occurring at the disk surfaces. Generally, surface modes, which are present only for sufficiently large radial wavenumbers, display higher growth rates than body modes. Furthermore, thermal stratification of the disk enhances the growth rates of both surface and body modes due to increased vertical shear, and amplifies the VSI-driven kinetic energy in the radial direction relative to the vertical direction.

This paper follows up on Paper I by conducting hydrodynamic simulations of thermally stratified disks susceptible to the VSI. This work is a straightforward extension of the isothermal models of Barraza-Alfaro et al. (2021) to disks with a vertical temperature gradient. We investigate the nonlinear consequences of the VSI in these stratified disks and assess the observability of a saturated turbulent state. We also explore how the optical depth of tracer molecules affects velocity residual maps in thermally stratified disks.

This paper is organized as follows: In Section 2, we describe our three-dimensional (3D) disk models and numerical methods. In Section 3, we present the results of our nonlinear simulations and the synthetic velocity residual maps at turbulence saturation. In Section 4, we discuss the contribution of each velocity component to the velocity residual maps and the effects of the optical depth of tracer molecules. Finally, we summarize our results in Section 5.

2. NUMERICAL METHODS

We adopt the same disk models as in [Paper I](#). We set the disk temperature as

$$T(R, Z) = \begin{cases} T_{\text{atm}}(R) + [T_{\text{mid}}(R) - T_{\text{atm}}(R)] \cos^2 \left(\frac{\pi Z}{2Z_q} \right), & \text{for } Z < Z_q, \\ T_{\text{atm}}(R), & \text{for } Z \geq Z_q, \end{cases} \quad (1)$$

where $T_{\text{mid}}(R) = 25.7(R/R_0)^{-1/2}$ K is the temperature in the midplane, with $R_0 = 100$ au being the reference radius, and T_{atm} is the temperature in the disk ‘‘atmosphere’’ located at $Z \geq Z_q$ ([Dartois et al. 2003](#)). We set the pressure scale height to $H = 10(R/R_0)^{5/4}$ au, and take $Z_q = 3H$. We consider three models with $n \equiv T_{\text{atm}}/T_{\text{mid}} = 1, 2, 3$, with $n = 1$ corresponding to the vertically isothermal disk.

Our disks are initially in hydrostatic equilibrium along the vertical direction, with the density distribution given by

$$\rho(R, Z) = \rho_0 \left(\frac{R}{R_0} \right)^{-9/4} \frac{c_s^2(R, Z)}{c_s^2(R, 0)} \times \exp \left[- \int_0^Z \frac{1}{c_s^2(R, Z')} \frac{\partial \Phi}{\partial Z'} dZ' \right], \quad (2)$$

where ρ_0 is the density at $(R, Z) = (R_0, 0)$, $c_s = (k_B T / \mu m_{\text{H}})^{1/2}$ is the isothermal speed of sound with the mean molecular weight $\mu = 2.3$, and $\Phi(R, Z) = -GM_*/(R^2 + Z^2)^{1/2}$ is the gravitational potential of the central star with mass $M_* = 1 M_{\odot}$. We take $\rho_0 \approx 0.018 M_* R_0^{-3}$, for which the total disk is 5% of the mass of the central star.

The radial force balance requires the angular velocity Ω of the disk rotation satisfies

$$\Omega^2(R, Z) = \Omega_K^2 \sin \theta + \frac{1}{\rho r \sin^2 \theta} \frac{\partial (c_s^2 \rho)}{\partial r}, \quad (3)$$

where $\Omega_K(R) = \sqrt{GM_*/R^3}$ is the Keplerian angular velocity, $\theta = \cos^{-1}(Z/r)$ is the polar angle, and $r = R/\sin \theta$ is the spherical radius. The vertical shear can be measured by the shear parameter defined as

$$q = -R \frac{\partial \ln \Omega}{\partial Z}. \quad (4)$$

As illustrated in [Figure 1\(d\)](#) of [Paper I](#), a disk with a larger n exhibits higher vertical shear. In the isothermal disk with $n = 1$, q increases approximately linearly with Z . In contrast, in the stratified disks with $n = 2$ and 3, q takes on a parabolic shape at $Z < Z_q$ where $\partial T / \partial z$ is positive, peaking at $Z \sim 0.5 Z_q$, and a linear trend

at $Z \geq Z_q$ where T is constant. The density-weighted vertically averaged shear parameter is $\langle q \rangle = 0.02, 0.06$, and 0.10 for the disk with $n = 1, 2$, and 3, respectively, suggesting that the VSI should be stronger in a disk with larger n .

We use FARGO3D ([Benítez-Llambay & Masset 2016](#)) to run 3D hydrodynamic simulations in spherical polar coordinate (r, θ, ϕ) by adopting a locally isothermal equation of state. Our computational domain is equal to that of [Barraza-Alfaro et al. \(2021\)](#), which spans r from 40 au to 250 au in the radial direction and θ ranging from $\pi/2 - \arctan(4.5H_0/R_0)$ to $\pi/2 + \arctan(4.5H_0/R_0)$ in the meridional direction, while covering the entire 2π radians in the azimuthal direction. Here, $H_0 = H(R_0) = 10$ au. The domain is discretized into (512, 128, 1024) cells in the (r, θ, ϕ) directions, respectively. We employ a logarithmic grid spacing in the radial direction with $\Delta r = 0.35$ au at $R = R_0$, while using linear spacing in both meridional and azimuthal directions with $\Delta \theta = H_0/(15.1R_0)$ and $\Delta \phi = 6.1 \times 10^{-2}$ radians. To seed perturbations for the VSI, we initially introduce random noises to the meridional velocity v_{θ} at the level of $\sim 10^{-6} c_s$.

At the meridional boundaries, we implement the zero-gradient boundary conditions for v_r and the reflecting boundary conditions for v_{θ} , while extrapolating ρ and v_{ϕ} on ghost cells from adjacent active cells. At the radial boundaries, we apply the reflecting boundary conditions for v_r and the zero-gradient boundary conditions for v_{θ} , and extrapolate ρ and v_{ϕ} . In addition, we establish wave-damping zones at $40 \text{ au} \leq r \leq 48 \text{ au}$ and $200 \text{ au} \leq r \leq 250 \text{ au}$ to prevent wave reflection ([de Val-Borro et al. 2006](#)). To ensure numerical convergence, we conduct additional simulations with halved grid spacing and various meridional boundary conditions. The results presented in [Appendix A](#) demonstrate that the numerical outcomes remain robust despite changes in resolution and boundary conditions.

3. RESULTS

In this section, we first describe the simulation results, focusing on the morphologies and the level of turbulence at saturation. We then present the synthetic observations of the model disks using various CO lines.

3.1. Hydrodynamic Simulations

[Figure 1](#) plots the evolutionary histories of the perturbed kinetic energy $\delta E_K \equiv \frac{1}{2} \int \rho (v_r^2 + v_{\theta}^2 + \delta v_{\phi}^2) dV$ relative to the initial kinetic energy $E_K(0) \equiv \frac{1}{2} \int \rho v_{\phi}^2 dV$ at $t = 0$ for all models as functions of t/t_{orb} . Here, $\delta v_{\phi} \equiv v_{\phi} - v_{\phi}(t = 0)$ is the perturbed azimuthal velocity and $t_{\text{orb}} = 2\pi/\Omega(R_0)$ is the orbital time at the

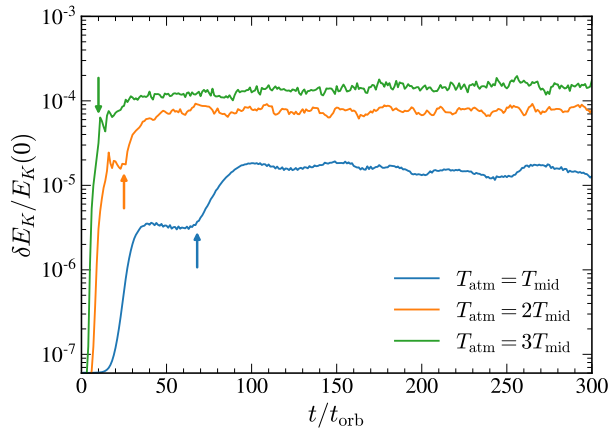


Figure 1. Temporal variations of the perturbed kinetic energy δE_K normalized by the initial kinetic energy $E_K(0)$ for models with $T_{\text{atm}}/T_{\text{mid}} = 0, 1, 2$. The initial increase in δE_K results from the growth of surface modes, while the subsequent growth phase, indicated by an arrow in each model, is driven by body modes.

reference radius. In each disk, the initial perturbations applied to v_θ induce wave motions in the gas. The system undergoes an initial relaxation phase as the waves propagate throughout the disk. Once the system picks up the most unstable VSI modes, δE_K begins to grow with time. This occurs at $t/t_{\text{orb}} \sim 15$ in the isothermal disk with $n = 1$, but much earlier at $t/t_{\text{orb}} \lesssim 3$ in the thermally stratified disks with $n = 2$ and 3.

According to Nelson et al. (2013), the VSI comprises two distinct modes: surface modes (or finger modes) which develop near the disk surfaces and body modes growing near the midplane. These surface modes typically have shorter radial wavelengths and undergo faster growth, while the body modes have longer radial wavelengths and slower growth rates (Paper I). In Figure 1, δE_K exhibits two discernible phases of exponential growth. In the isothermal disk with $n = 1$, δE_K exhibits an initial exponential growth (at $15 \lesssim t/t_{\text{orb}} \lesssim 30$) and saturation (at $t/t_{\text{orb}} \sim 30$) of the surface modes. The perturbations induced by the surface modes propagate toward the midplane, thereby exciting body modes. The slower-growing body modes begin to dominate at $t/t_{\text{orb}} \sim 70$, indicated by the blue arrow in Figure 1, causing a further increase in δE_K around $t/t_{\text{orb}} \sim 70$ – 100 , ultimately saturating at $\delta E_K/E_K(0) \sim 10^{-5}$. As the disk becomes thermally stratified, both surface and body modes grow more rapidly, and the interval between the first and second growth phases of δE_K shortens. In the $n = 2$ disk, the saturation of the surface modes occurs at $t/t_{\text{orb}} \sim 20$, with body modes beginning to dominate at $t/t_{\text{orb}} \sim 25$. In contrast, in the $n = 3$ disk, the body modes dominate as early as $t/t_{\text{orb}} \sim 10$, even

before the surface modes saturate. The saturated level of δE_K is also higher in a more thermally stratified disk.

To analyze the impact of thermal stratification on the VSI in detail, we examine the induced velocity perturbations. Figure 2 presents snapshots of the meridional velocity v_θ in the R – Z plane at selected epochs. Two notable differences emerge between the isothermal and thermally stratified disks. Firstly, the growth of the VSI is relatively slow in the isothermal disk. However, in thermally stratified disks, the initial relaxation phase is brief, and the VSI grows more rapidly, reaching turbulence saturation sooner. Secondly, while the VSI initially arises near the disk surfaces in the isothermal disk, in stratified disks, it emerges in regions with $|Z| \approx 0.5Z_q$, where the vertical shear is the strongest. This is most clearly seen in the $n = 3$ model. Over time, the regions experiencing significant growth of the VSI extend radially outward, leading to an increase in the perturbed velocities. Concurrently, the VSI modes propagate from the surfaces to the midplane, engaging in nonlinear interactions with modes propagating from opposite sides and different radii. These nonlinear interactions among VSI modes drive the disk into a highly turbulent state.

As shown in the left panels of Figure 2, the radial wavelength of the dominant VSI mode in a thermally stratified disk is longer than that in the vertically isothermal disk. To estimate the most susceptible wavelength of the VSI during the linear phase in the simulations, we take the data for the vertical momentum ρv_z at the times shown in the left panels of Figure 2, which allows to capture the initial growing phase of the VSI. We measure the radial distances between two consecutive zeros of ρv_z at $Z/H = Z_q/2$ and set it equal to half of the radial wavelength λ_R (see, e.g., Svanberg et al. 2022). Figure 3 plots the radial distributions of λ_R/H as functions of R . Our best fits are

$$\frac{\lambda_R}{H} = \begin{cases} 3.31(R/R_0 - 0.43), & \text{for } n = 1, \\ 7.18(R/R_0 - 0.43), & \text{for } n = 2, \\ 10.7(R/R_0 - 0.43), & \text{for } n = 3. \end{cases} \quad (5)$$

Note that the radial wavelength goes to zero at $R/R_0 = 0.43$ due to the wave-damping zone applied at the inner radial boundary. A more thermally stratified disk has longer λ_R due to stronger shear, which is consistent with Equation (10) of Paper I for fixed $k_z H \sim 1$. The increasing trend of λ_R with R in the linear growth phase is also similar to the numerical results of Svanberg et al. (2022) in the nonlinear regime.

Figures 4 and 5 present the face-on distributions of the density and velocity at $z/H = 0$ and 3, respectively, while Figure 6 plots the edge-on distributions of

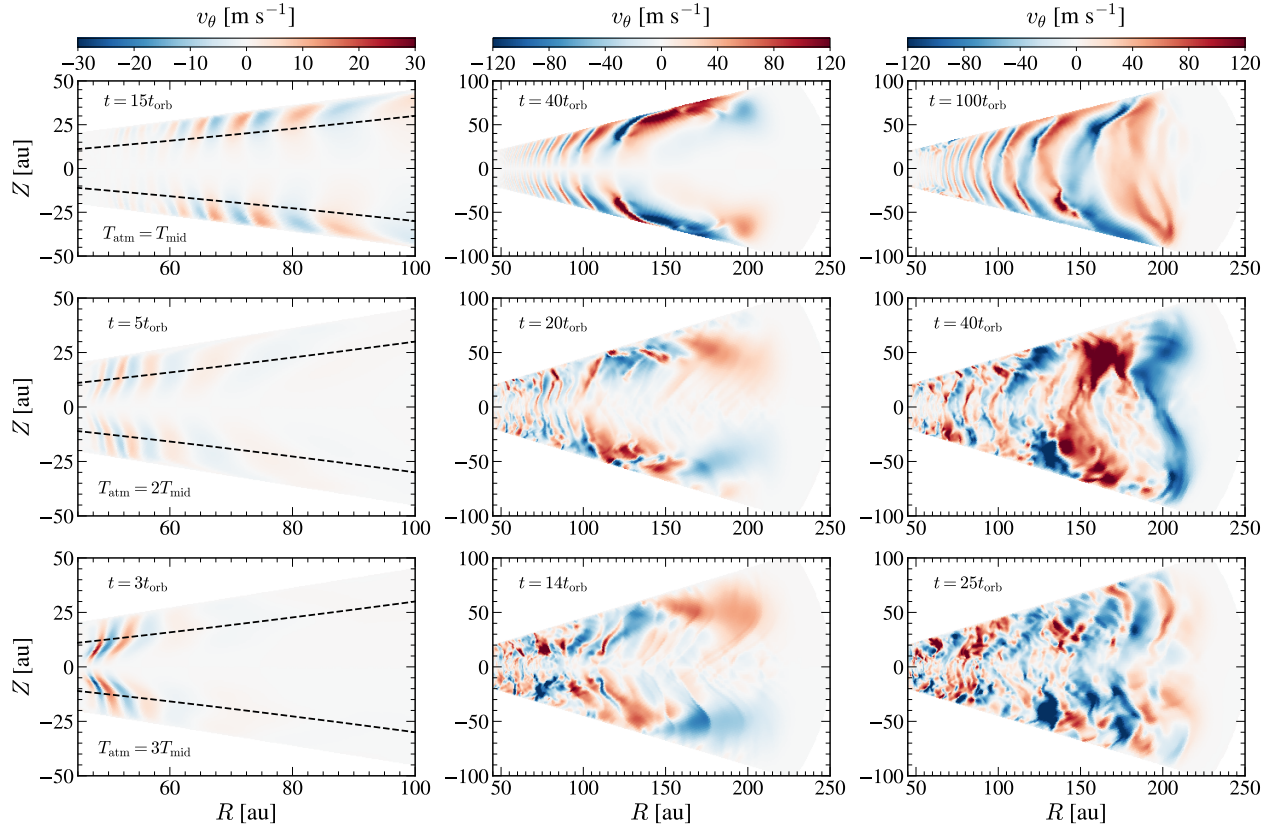


Figure 2. Snapshots of the meridional velocity v_θ in the R - Z plane at selected times. Each row corresponds to the models with $n = 1, 2,$ and 3 from top to bottom, respectively. The dashed lines in the first column marks the height with $|Z| = Z_q$. In all models, VSI perturbations grow fastest near the disk atmospheres at smaller radii in the early stages. The VSI-unstable modes have higher growth rates and longer radial wavelengths in disks with stronger thermal stratification.

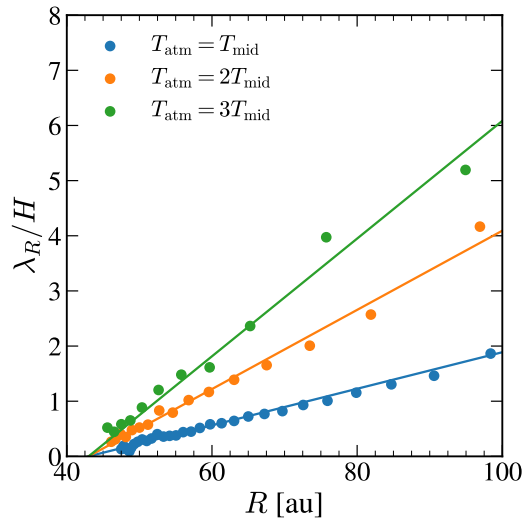


Figure 3. Radial wavelengths λ_R of the VSI measured at the times shown in the left panels of Figure 2. The solid lines are the best fits described by Equation (5), indicating that λ_R is longer at larger R and in a more thermally stratified disk.

the azimuthally-averaged quantities, all at $t/t_{\text{orb}} = 300$. Each column shows the perturbed density $\delta\rho$ and radial velocity v_r , meridional velocity v_θ , and perturbed azimuthal velocity δv_ϕ from left to right. Each row corresponds to the model with $n = 1, 2,$ and 3 from top to bottom. Clearly, the perturbations induced by the VSI are more pronounced at higher $|z|$ and in disks with greater thermal stratification. Additionally, structures of the VSI-induced turbulence in the stratified disks are more complex compared to those in the vertically isothermal disk.

As Figures 4 and 5 show, the meridional and azimuthal components of the perturbed velocities exhibit quasi-axisymmetric ring-like structures, reflecting the axisymmetric nature of the VSI (Nelson et al. 2013; Stoll & Kley 2014; Paper I). This in turn implies that the perturbed azimuthal velocity is smaller than the other components. Since the VSI is incompressible and has $|v_r/v_\theta| \sim |k_z/k_x| \sim q$ (Paper I), the density and radial velocity perturbations are weaker than the other perturbations. In the isothermal disk, the maximum amplitudes of the time-averaged velocity perturbations

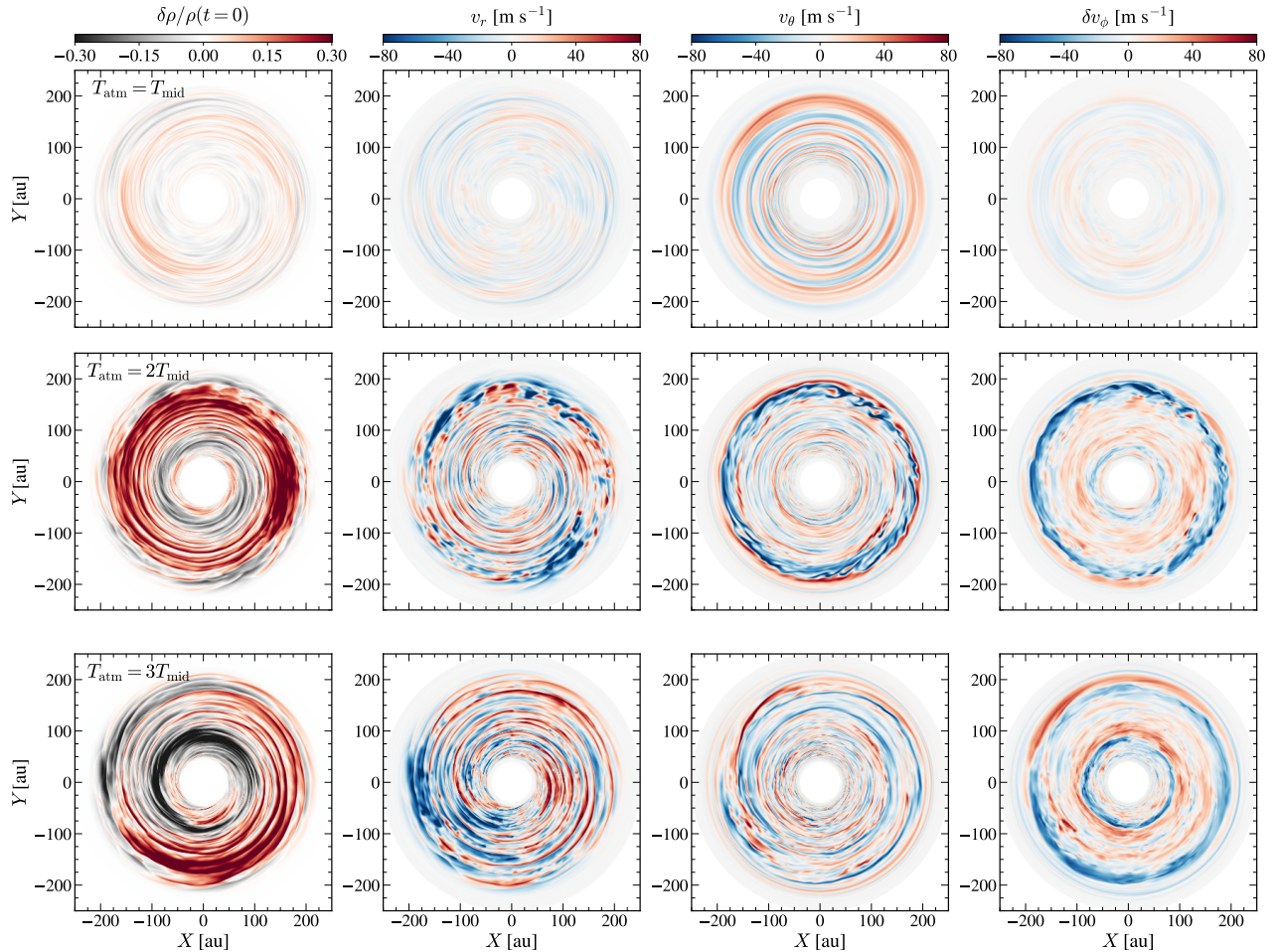


Figure 4. Distributions of the perturbed quantities at the midplane at $t/t_{\text{orb}} = 300$. Each column represents the perturbed density $\delta\rho \equiv \rho - \rho(t=0)$, radial velocity v_r , meridional velocity v_θ , and perturbed azimuthal velocity $\delta v_\phi \equiv v_\phi - v_\phi(t=0)$ from left to right, respectively. Each row corresponds to the model with $n = 1, 2$, and 3 from top to bottom, respectively. The VSI-induced perturbations are stronger in disks with a higher degree of thermal stratification. While the velocity perturbations are predominantly meridional in the isothermal disk, the thermally stratified disk exhibits significant perturbations in the radial and azimuthal velocities as well.

after saturation in the midplane are $21, 57$, and 15 m s^{-1} in the radial, meridional, azimuthal directions, respectively. These increase to $82, 95$, and 50 m s^{-1} in the $n = 2$ disk and $123, 116$, and 73 m s^{-1} in the $n = 3$ disk. The corresponding ratio of the perturbed velocities is $|v_r/v_\theta| \sim 0.4, 0.9$, and 1.1 and $|\delta v_\phi/v_\theta| \sim 0.3, 0.5$, and 0.6 in the disk with $n = 1, 2$, and 3 , respectively. Although the trend of $|v_r/v_\theta|$ increasing with n aligns with the finding of Paper I, the velocity ratio is quantitatively larger than the linear prediction, likely due to the combined effect of gas compressibility, nonlinear wave interactions, and other factors. Additionally, it is possible that the VSI in thermally stratified disks grows sufficiently to excite the parasitic instabilities of the Kelvin–Helmholtz type, resulting in the formation

of vortices within the disk plane (Latter & Papaloizou 2018).

Barraza-Alfaro et al. (2021) found that the presence of the quasi-axisymmetric rings in the distributions of v_θ is crucial for detecting the VSI-induced turbulence. We note that thermal stratification not only enhances the level of turbulence but also reduces the number of ring-like features. This reduction is due to the fact that strong vertical shear favors long radial wavelengths for growth (Equation 10 of Paper I). Also, the non-monotonic q profile in the $n = 2, 3$ disks makes the radial and vertical wavelengths of the VSI modes vary throughout the disk, making it harder for coherent structures to develop.

To find out the height where the VSI is strongest, we plot in Figure 7 the Reynolds stresses $T_{R\phi} \equiv \langle \rho v_R v_\phi \rangle -$

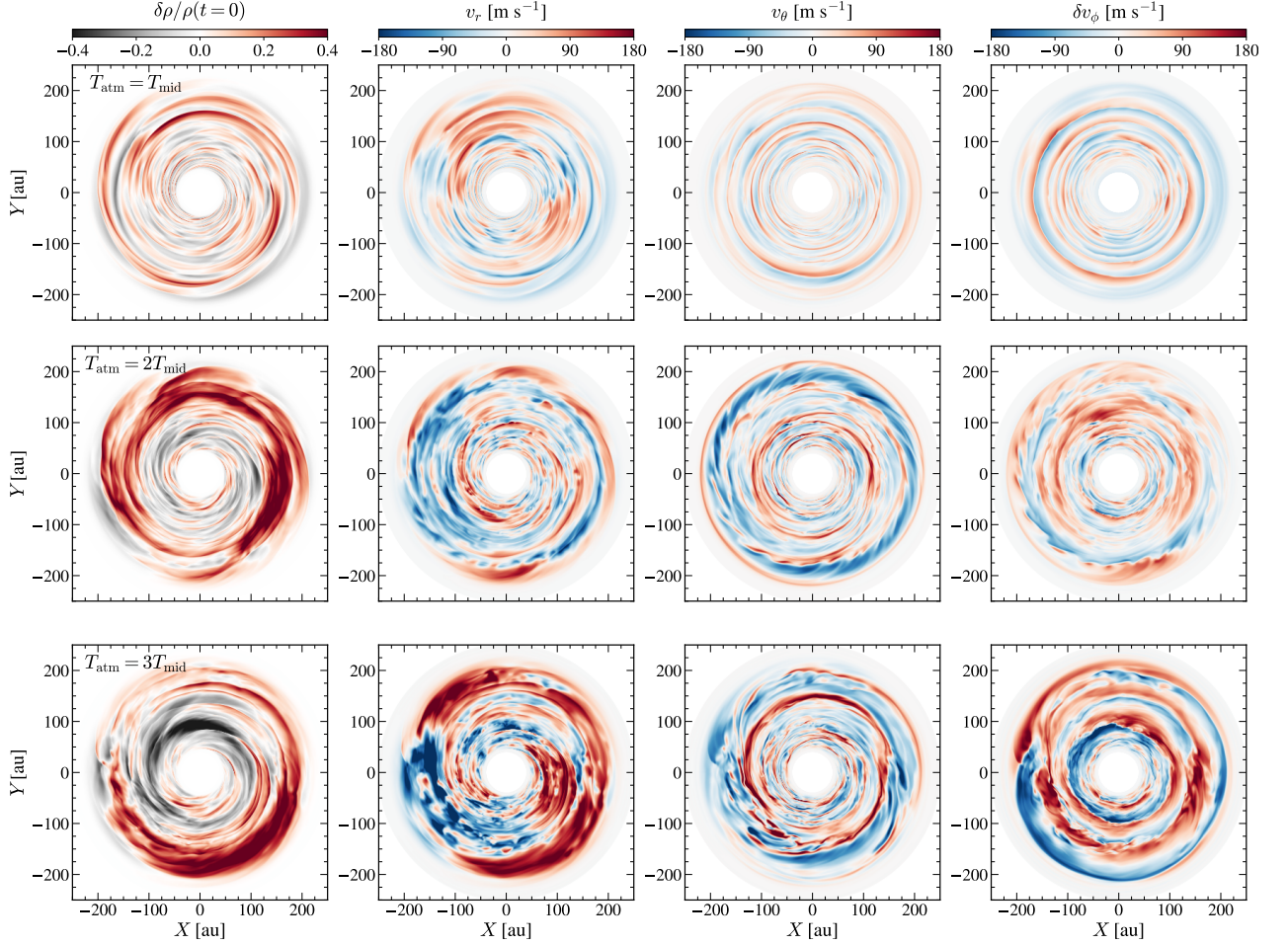


Figure 5. Same as Figure 4 but depicted at the high-altitude region with $z = 3H$.

$\langle v_\phi \rangle \langle \rho v_R \rangle$ and $T_{Z\phi} \equiv \langle \rho v_Z v_\phi \rangle - \langle v_\phi \rangle \langle \rho v_Z \rangle$, normalized by the thermal pressure $P = \rho c_s^2$ at $r = 100$ au, as functions of the polar angle. Here, $\langle f \rangle$ denotes the average of the quantity f over $r = 80\text{--}120$ au, $\phi = 0\text{--}2\pi$, and $t = 150\text{--}300 t_{\text{orb}}$. Clearly, $T_{R\phi}$ is more or less symmetric with respect to the midplane, while $T_{Z\phi}$ is antisymmetric (e.g., Zhang et al. 2024). Thermal stratification increases the level of both $T_{R\phi}$ and $T_{Z\phi}$. In particular, a higher value of $T_{R\phi}$ at the disk midplane suggests an enhanced radial gas inflow in a more thermally stratified disk, consistent with Zhang et al. (2024). In addition, thermal stratification shifts the regions of maximum $T_{Z\phi}$ toward $|Z| \sim Z_q/2$, where shear is strongest.

To quantify the level of turbulence driven by the VSI, we calculate the ratio of the volume-averaged Reynolds stress, $T_{R\phi}$, to the volume-averaged thermal pressure as

$$\alpha_{R\phi} \equiv \frac{\int T_{R\phi} dV}{\int P dV}, \quad (6)$$

Figure 8 plots temporal changes of $\alpha_{R\phi}$ for our models. In the isothermal disk, $\alpha_{R\phi}$ exhibits a dramatic increase

until $t/t_{\text{orb}} \sim 60$ when the growth of the surface modes saturates. Subsequently, it grows more slowly, as the body modes develop, increasing the turbulence level. It eventually saturates at $t/t_{\text{orb}} \sim 200$ when the turbulence is fully developed in the disk, reaching a level of $\alpha_{R\phi} \sim 1 \times 10^{-4}$, consistent with the results of Barraza-Alfaro et al. (2021). In the thermally stratified disks, the VSI begins to grow earlier and faster than in the isothermal disk. The phase of slowly increasing $\alpha_{R\phi}$ is brief, as well. The saturated level of VSI-driven turbulence is $\alpha_{R\phi} \sim 1 \times 10^{-3}$ and 2×10^{-3} for the disk with $n = 2$ and 3, respectively.

3.2. Synthetic Observations

We turn our attention to examining the observability of PPDs with turbulent motions driven by the VSI in thermally stratified disks, by creating synthetic images of molecular lines emitted from the model disks. For this purpose, we post-process the simulation data at the end of the runs ($t/t_{\text{orb}} = 300$) using the Monte-Carlo radiative transfer code RADMC3D (Dullemond

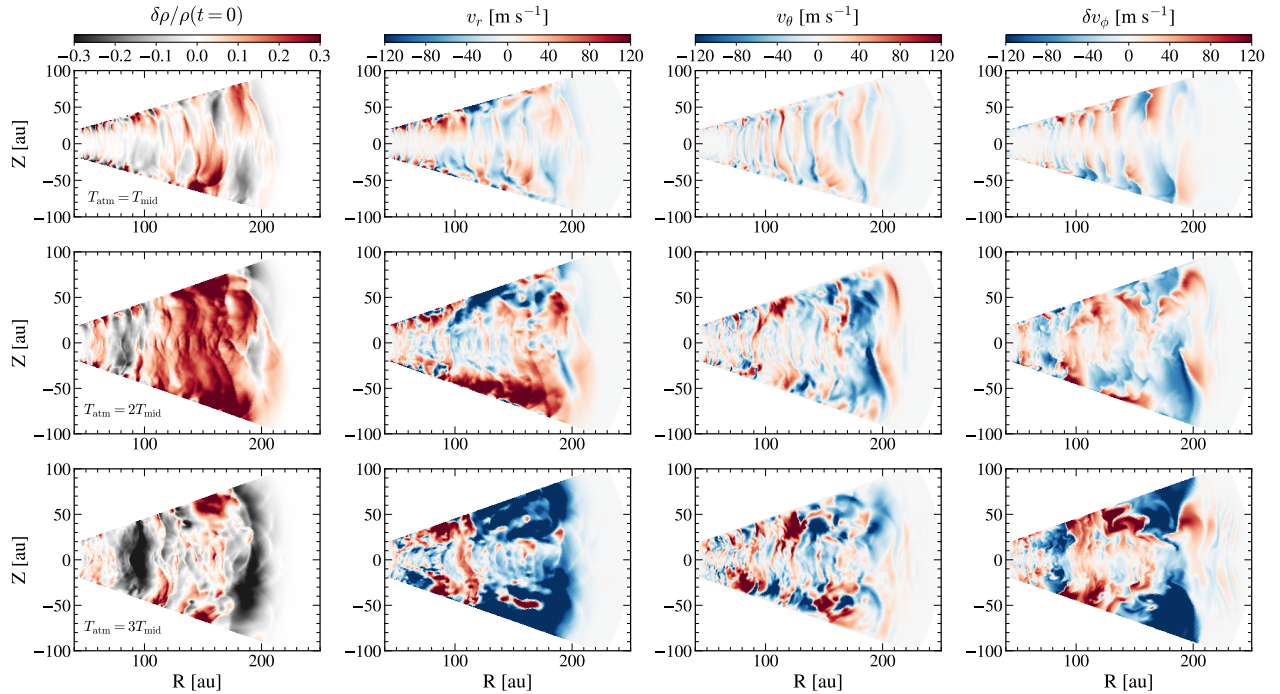


Figure 6. Distributions of the perturbations in the R - Z plane at $\phi = 0$ when $t/t_{\text{orb}} = 300$. The panel layout is the same as in Figure 4. The turbulence driven by the VSI is generally stronger at the surface compared to the midplane and also in a model with a larger degree of thermal stratification.

et al. 2012). We calculate the line-of-sight velocity maps from synthetic channel maps of ^{12}CO , ^{13}CO , and C^{18}O $J = 2 - 1$ transitions with central frequencies at approximately 230.538 GHz, 220.399 GHz, and 219.560 GHz, respectively.

We assume a molecular abundance of ^{12}CO to be 1.0×10^{-4} relative to H_2 and calculate the abundances of ^{13}CO and C^{18}O by adopting the isotope ratios $[^{12}\text{C}]/[^{13}\text{C}] \sim 77$ and $[^{16}\text{C}]/[^{18}\text{O}] \sim 560$ in the interstellar medium (Wilson & Rood 1994). We then create the 3D data cubes for the CO number density and the three velocity components from the simulation data. Using the information for CO lines from the LAMDA database (Schöier et al. 2005) we construct the molecular line emission images of the model disks.

We consider three inclination angles $i = 5^\circ$, 20° , and 35° of the disk relative to the line of sight, while fixing the position angle at 90° and the distance to the disk at 100 pc. The synthetic cubes have a total bandwidth of 6 km s^{-1} and 120 channels with resolution of 0.05 km s^{-1} . To assess the observability of the VSI signatures, we convolve the data with a circular Gaussian beam with a full-width at half maxi-

mum (FWHM) of $0.1''$ and add root-mean-square noise of $\sim 1.5 \text{ mJy beam}^{-1}$ using SYNDISK¹.

After constructing the synthetic channel maps, we take the following steps to extract kinematic information of the observed PPDs. We derive the velocity centroid map from the synthetic images using BETTERMOMENTS² (Teague & Foreman-Mackey 2018). At each pixel, we fit the line profile using a Gauss-Hermite function to obtain the line-of-sight velocity distribution of the disk. Subsequently, we utilize EDDY³ (Teague 2019) along with the Keplerian disk model (outlined below) to subtract it from the velocity centroid, v_0 , thereby isolating the velocity perturbations.

We follow the methodology outlined by Barraza-Alfaro et al. (2021) to construct the Keplerian disk model, v_{mod} , as follows. We first project the Keplerian

¹ <https://github.com/richteague/syndisk>

² <https://github.com/richteague/bettermoments>

³ <https://github.com/richteague/eddy>

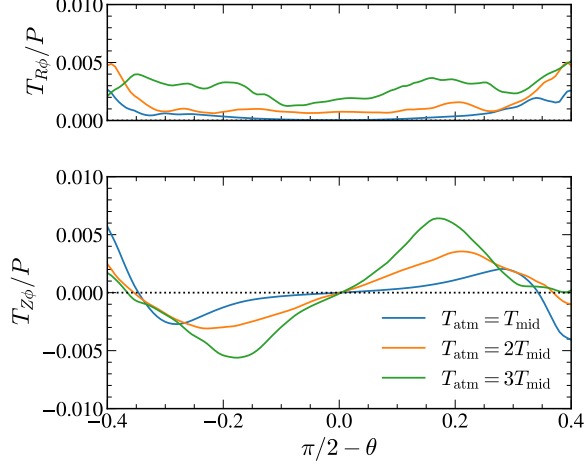


Figure 7. Vertical distributions of the R - ϕ and Z - ϕ Reynolds stresses, normalized by the thermal pressure at $r = 100$ au. Thermal stratification not only increases $T_{R\phi}$ and $T_{Z\phi}$ but also shifts the regions of maximum $T_{Z\phi}$ toward $|Z| \sim Z_q/2$, where shear is strongest.

velocity onto the plane of the sky, given by

$$v_\phi = v_{\phi,100} \left(\frac{R}{100 \text{ au}} \right)^{q_\phi}, \quad (7)$$

$$v_R = v_{R,100} \left(\frac{R}{100 \text{ au}} \right)^{q_R}, \quad (8)$$

$$v_{\text{mod}} = v_{\text{LSR}} + v_\phi \cos \varphi \sin i + v_R \sin \varphi \sin i, \quad (9)$$

where $v_{\phi,100}$ and $v_{R,100}$ are the azimuthal and radial velocity of the disk at 100 au from the central star, respectively, with the power-law slope of q_ϕ and q_R . In Equation (9), v_{LSR} represents the systematic velocity of the disk and φ is the polar angle measured east of north relative to the red-shifted major axis. Additionally, we account for the effect of the elevated emission surface by adopting the approach of Law et al. (2021), who define the CO emission surface as

$$\tilde{z}(\tilde{R}) = \tilde{z}_0 \left(\frac{\tilde{R}}{1''} \right)^\Psi \exp \left(- \left[\frac{\tilde{R}}{\tilde{R}_{\text{taper}}} \right]^{q_{\text{taper}}} \right), \quad (10)$$

where $\tilde{z}_0 = \tilde{z}(\tilde{R} = 1'')$ and Ψ describes the flaring of the emission surface, and \tilde{R}_{taper} and q_{taper} parameterize the tapering of the emission surface at the disk edges. Here, all quantities denoted with a tilde are expressed in units of arcseconds.

Employing a series of Markov Chain Monte Carlo models consisting of 128 walkers and 2000 burn-in steps, we identify the Keplerian disk model that best aligns with the obtained velocity centroid v_0 . We iterate over a set of 13 parameters: the position of disk

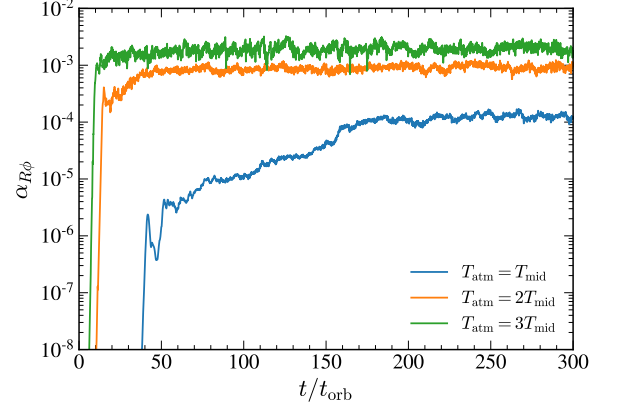


Figure 8. Temporal evolution of the Reynolds stress-to-pressure ratio, $\alpha_{R\phi}$. At the end of the simulation, the thermal stratification increases $\alpha_{R\phi}$ by a factor of ~ 10 and ~ 20 in the disk with $n = 2$ and 3, respectively, compared to the isothermal disk.

center, disk position angle, velocity profile parameters ($v_{\text{LSR}}, v_{\phi,100}, v_{R,100}, q_\phi, q_R$), and emission surface parameters ($\tilde{z}_0, \Psi, \varphi, \tilde{R}_{\text{taper}}, q_{\text{taper}}$). We keep the distance to the source at 100 pc and adopt the same disk inclination angle as in the synthetic image. To mitigate potential contamination from emissions originating from the far side of the disk, we confine the radial range to $[0.55'', 2.0'']$, $[0.58'', 1.85'']$, and $[0.6'', 1.7'']$ for $i = 5^\circ, 20^\circ$, and 35° , respectively. Additionally, we apply a mask to the velocity residual to remove the outer regions of the image that are added only during the synthetic observation process and are irrelevant to the actual motion of the disk.

Figure 9 plots the observed maps of the velocity residual, $v_0 - v_{\text{mod}}$, of synthetic $^{12}\text{CO } J = 2 - 1$ molecular lines for differing inclinations $i = 5^\circ, 20^\circ$, and 35° from left to right. Each row corresponds to the disk with $n = 1, 2$, and 3 from top to bottom. The emergence and nonlinear saturation of the VSI induce deviations in the velocity fields from the Keplerian rotation. These velocity deviations are more pronounced in a disk with stronger thermal stratification. For instance, at an inclination angle of $i = 20^\circ$, the maximum amplitudes of residual velocities reach approximately 50, 80, and 100 m s^{-1} in disks with $n = 1, 2$, and 3, respectively.

The shape of VSI perturbations in velocity residual maps is crucial for identifying the presence of the VSI in kinematic observations (Pinte et al. 2023). In the isothermal disk, velocity deviations from VSI perturbations appear as quasi-axisymmetric rings at low inclinations ($i \leq 20^\circ$). The velocity residual map at $i = 35^\circ$, shown in the top-right panel of Figure 9, displays axisymmetric rings alongside spoke-like radial fea-

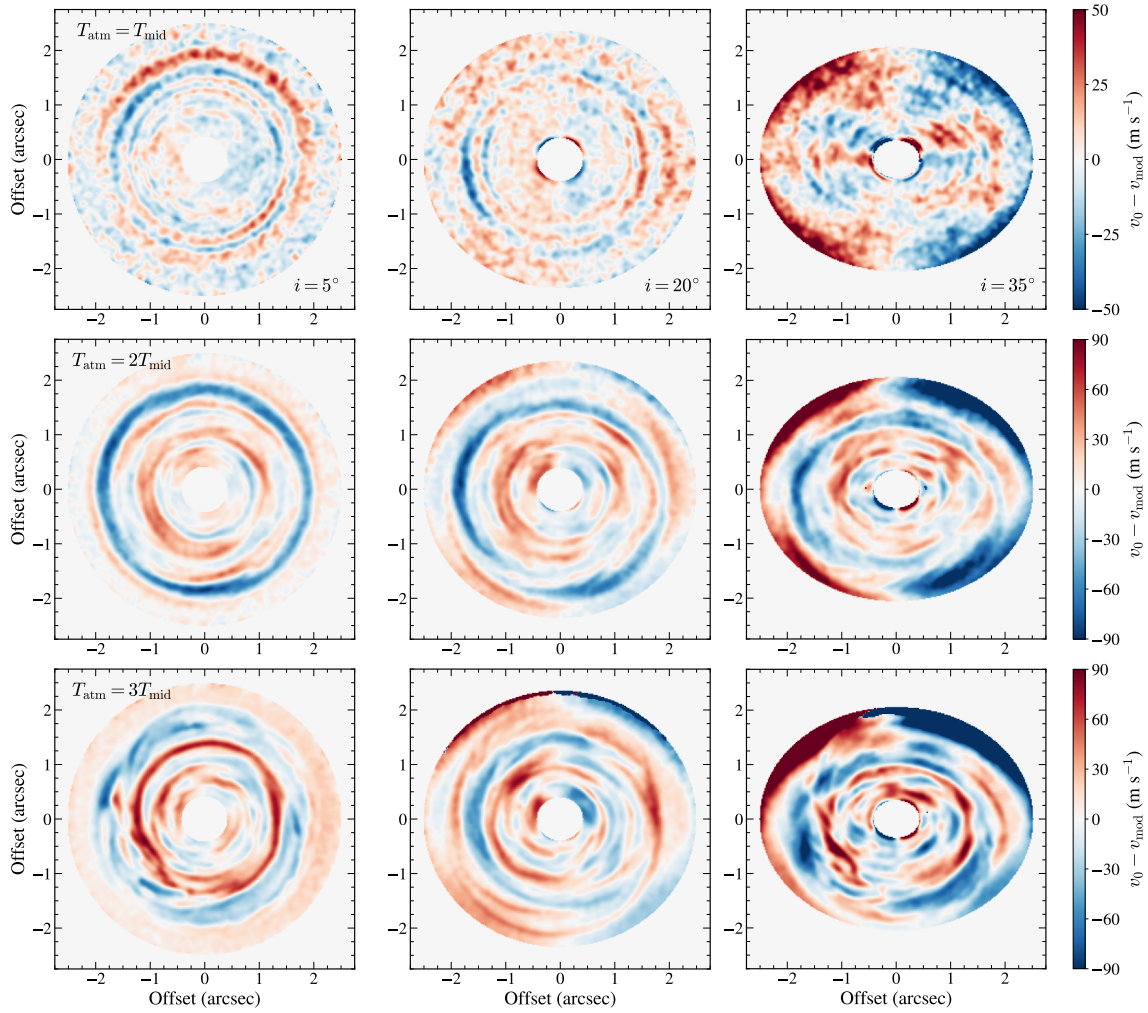


Figure 9. Distributions of the residual velocity, $v_0 - v_{\text{mod}}$, of synthetic $^{12}\text{CO } J = 2 - 1$ lines, observed by a circular beam with FWHM of $0.10''$ after adding a root-mean-square noise of $\sim 1.5 \text{ mJy}$. Each row corresponds to the disk with $n = 1, 2, 3$ from left to right, while each column is for the inclination angle of $i = 5^\circ, 20^\circ, 35^\circ$ from top to bottom.

tures. These radial structures are most likely due to discrepancies between the true and fitted emission surfaces (Barraza-Alfaro et al. 2021). Notably, recovering the emission surface and rotation velocity becomes increasingly challenging as the inclination rises.

In thermally stratified disks, the VSI-induced perturbations in velocity residual maps exhibit greater complexity compared to their isothermal counterparts. Figure 9 shows that in such disks, velocity perturbations appear as ring segments even at low disk inclinations. This behavior arises from the non-monotonic distribution of the vertical shear q , which suppresses the development of coherent structures, as shown in Figures 4 and 5. Vortices generated by the Kelvin-Helmholtz-like parasitic instability further contribute to breaking quasi-axisymmetric rings into segments. Although the complex shapes of VSI perturbations in thermally stratified disks can make detection challenging, the strong as-

sociated velocity deviations allow them to remain visible at inclinations as high as $i = 45^\circ$. This contrasts with the isothermal disk, where VSI-induced perturbations are dominated by the vertical component, whose contribution to the line-of-sight velocity decreases at high inclinations (see Section 4.1 for discussion). For instance, Figure 10 shows the velocity residual map for the $n = 3$ disk at $i = 45^\circ$, revealing several ring segments.

4. DISCUSSION

We here discuss the contribution of each velocity component to the line-of-sight velocity and examine the effect of the optical depth of a tracer element through synthetic observations from different CO isotopologues. We also remark a few caveats that need to be considered in future studies.

4.1. Contribution of Each Velocity Component

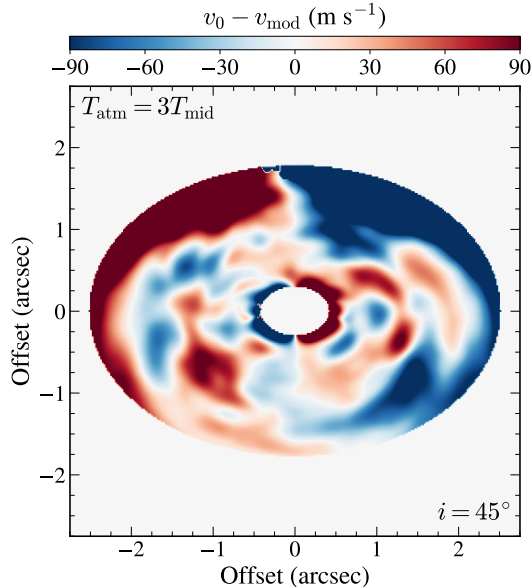


Figure 10. Velocity residual map for the $n = 3$ disk viewed at an inclination of $i = 45^\circ$. Several ring segments generated by VSI perturbations are visible in the molecular line emission image.

Barraza-Alfaro et al. (2021) demonstrated that the velocity deviations in their velocity residual maps for vertically isothermal disks are primarily due to the meridional velocity. As mentioned in Section 3.1, our thermally stratified disks have almost comparable velocities in the radial and vertical directions, and about half smaller velocities in the azimuthal direction. To quantify the contribution of each velocity component to the total deviations, we create the data cubes where only one velocity component is taken from the simulations, while the other two components are set equal to the initial conditions (i.e., without perturbations).

Figure 11 plots the resulting velocity residual maps at an inclination of $i = 35^\circ$. From left to right, each panel shows the maps generated when only v_r , v_ϕ , or v_θ is extracted from the simulations, respectively. Each row is for the model with $n = 1, 2, 3$ from top to bottom. The maximum values of $|v_0 - v_{\text{mod}}|$ are $\sim 35, 35,$ and 34 m s^{-1} when the perturbed component is $v_r, v_\theta,$ and v_ϕ , respectively, in the isothermal disk. These values change to $\sim 47, 48,$ and 31 m s^{-1} in the $n = 2$ disk, and $\sim 63, 55,$ and 58 m s^{-1} in the $n = 3$ disk. At $i = 35^\circ$, all three components of velocity perturbations are comparable in magnitude. At higher inclinations, however, the relative contributions of v_r and v_ϕ become increasingly dominant compared to v_θ .

4.2. Effect of the Optical Depth

For molecular line observations, probing the vertical disk structure is feasible using various isotopologues with different optical depths. Figure 12 illustrates the heights at which the optical depth of the CO isotopologues reaches unity when observed along the Z -direction in the disks with $n = 1, 2, 3$ from top to bottom, respectively. Given its higher abundance, ^{12}CO predominantly traces regions near the disk surfaces, whereas the less abundant C^{18}O primarily probes regions closer to the midplane.⁴ In addition, ^{13}CO and C^{18}O are effective in tracing deeper regions within a more thermally stratified disk due to the steeper density profile in the vertical direction (see Figure 1 of Paper I).

Figure 13 compares the velocity residual maps for ^{12}CO , ^{13}CO , and C^{18}O observations from left to right. The top and bottom panels correspond to the disks with $n = 1$ and 3 , respectively, utilizing the same set of parameters as in Figure 9. It is apparent that for the isothermal disk, the effect of the optical depth on the velocity residual is not significant, consistent with the result of Barraza-Alfaro et al. (2021). This is because the meridional velocity perturbation by the VSI in vertically isothermal disks does not exhibit strong height dependence (see the top panels of Figure 6). In the thermally stratified disks, however, the strength of VSI-induced features noticeably decreases going from ^{12}CO to C^{18}O . This is attributed to C^{18}O tracing regions close to the midplane, while the regions with high- $|Z|$ experience strong shear and thus are more susceptible to VSI in thermally stratified disks.

While the kinematic features of MWC 480 presented in Teague et al. (2021) resemble the quasi-axisymmetric rings generated by VSI perturbations, they cannot be fully explained by simulation results of Barraza-Alfaro et al. (2021) for a vertically isothermal disk. This discrepancy arises because the observed features exhibit a height dependence, with perturbations weakening closer to the midplane, and because they have a longer length scale than the synthetic images produced by vertically isothermal disk models. Thermal stratification, however, can resolve both issues by increasing the length scale of VSI perturbations and introducing a height-dependent morphology. This suggests that the ring structures observed in MWC 480 may indeed originate from the VSI.

4.3. Comparison with Other Mechanisms

In Section 3.2, we have demonstrated that VSI-driven velocity perturbations can be observed with ALMA and

⁴ Physical quantities probed by ^{12}CO may be subject to the adopted boundary conditions.

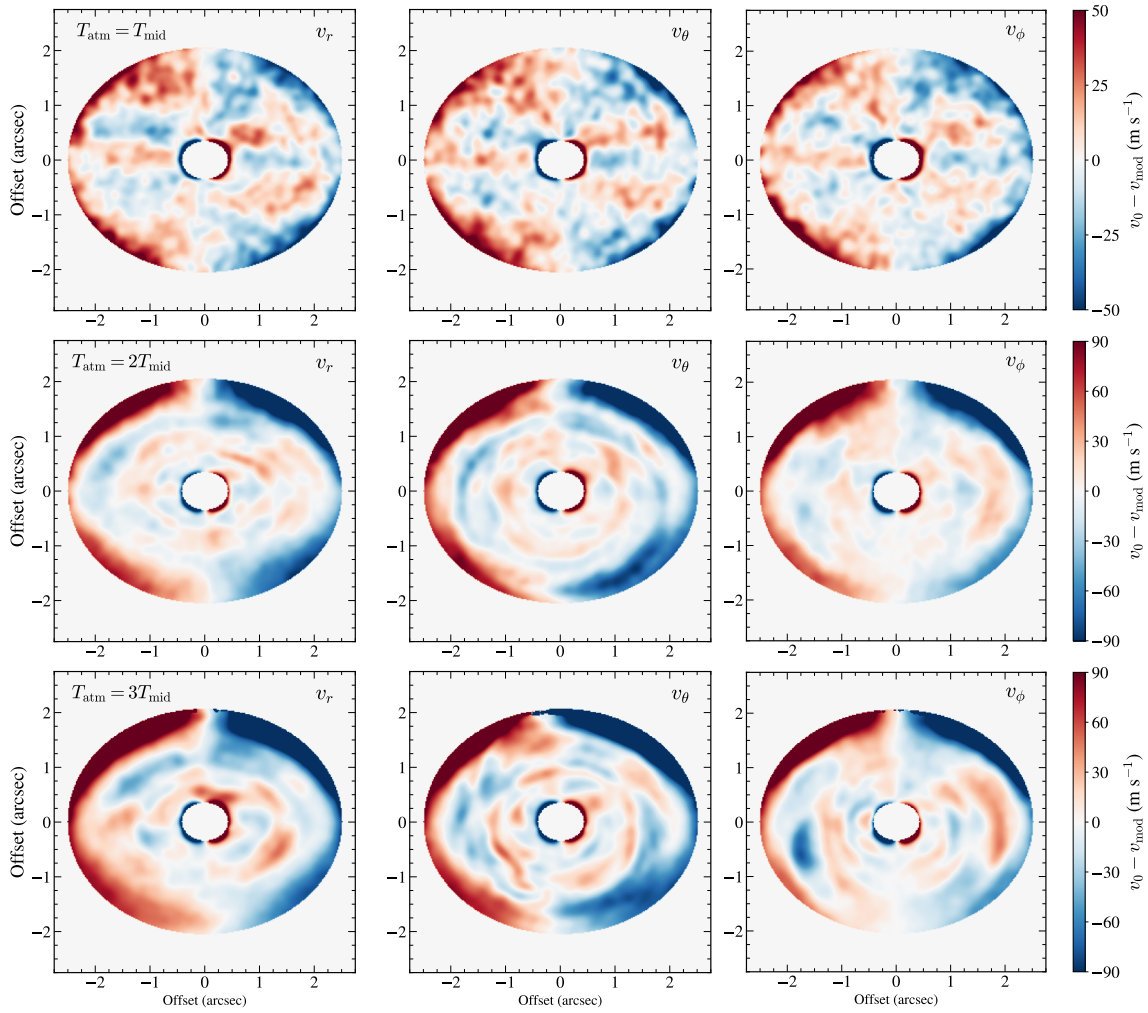


Figure 11. Contributions of (left) v_r , (middle) v_θ , and (right) v_ϕ to the velocity residual, $v_0 - v_{\text{mod}}$, for an inclination of $i = 35^\circ$. Each row corresponds to the disk with $n = 1, 2, 3$ from top to bottom. The contributions of all three velocity components are comparable at this inclination.

that their strength is enhanced by thermal stratification. However, other mechanisms can also produce similar large-scale gas motions in PPDs. Notable mechanisms include planet-disk interactions (Disk Dynamics Collaboration et al. 2020; Pinte et al. 2023) and vortices (Huang et al. 2018; Robert et al. 2020), although the resulting structures exhibit distinct kinematic features compared to those of the VSI.

First, VSI-induced features are global in the sense that they span large radial and azimuthal ranges. They appear as quasi-symmetric rings in vertically isothermal disks and ring segments in thermally stratified disks. Planet-induced spirals are also global but involve localized velocity kinks at the planet’s position (Perez et al. 2015; Pinte et al. 2019). Second, VSI-induced perturbations in thermally stratified disks are strongest in high- $|Z|$ regions, whereas planet-induced spirals are more prominent in the midplane. Third, vortices gener-

ated, for example, by the Rossby instability are local, appearing in a few channel maps, while VSI perturbations are present in multiple channel maps with similar magnitudes. Therefore, distinguishing the VSI signatures will require a closer examination of the velocity residual maps to find unique kinematic features of alternative scenarios.

4.4. Caveats

While our study presents the enhancement of the VSI perturbations due to thermal stratification, we note that our disk models are inviscid and isothermal, which is an ideal condition for the growth of the VSI. Previous studies have shown that the inclusion of viscosity (Nelson et al. 2013), finite cooling time (Lin & Youdin 2015), vertical buoyancy (Lin & Youdin 2015; Latter & Papaloizou 2018), and magnetic fields (Latter & Papaloizou 2018) can stabilize the VSI and weaken the re-

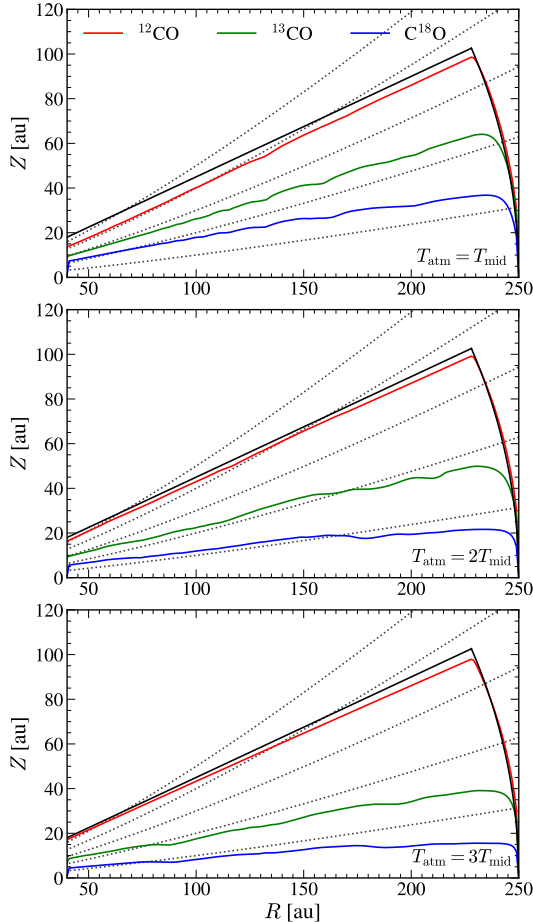


Figure 12. Locations of the emission surface with an optical depth of unity, observed along the Z -axis, for ^{12}CO (red), ^{13}CO (green), and C^{18}O (blue) lines in the disks with $n = 1, 2, 3$ from top to bottom. The solid black line denotes the simulation domain, while the dotted lines indicate the height with $Z/H = 1, \dots, 5$.

sulting velocity perturbations. Recent numerical studies with vertically varying cooling time (Fukuhara et al. 2023; Pfeil et al. 2023) and radiation hydrodynamic simulations of irradiated disks (Melon Fuksman et al. 2024; Zhang et al. 2024) commonly found the VSI is damped in the optically-thick, cold regions where the cooling time is longer than the critical cooling time. So, we expect that the amplitudes of VSI perturbations presented in this study is likely to be upper limits compared to the ones in real disks.

In addition, various non-axisymmetric features produced by a massive embedded planet can interfere with VSI-driven turbulence, making it difficult to distinguish between perturbations caused solely by the VSI and those originating from the planet (see also Ziampras et al. 2023; Barraza-Alfaro et al. 2024). Depending on the planet mass, the planet-induced spiral wakes or a

gap can disrupt or damp the VSI perturbations, especially in the disk midplane (Barraza-Alfaro et al. 2024).

5. CONCLUSION

In this paper, we investigate the effects of vertical thermal stratification on the nonlinear turbulent motions induced by the VSI in PPDs. We consider three disk models in hydrostatic equilibrium, characterized by $n = T_{\text{atm}}/T_{\text{mid}} = 1, 2, 3$: $n = 1$ represents an isothermal disk, while $n = 2$ and 3 correspond to thermally stratified disks. We study their nonlinear evolution by conducting 3D hydrodynamic simulations. Once the disks reach a turbulent state at saturation, we generate various synthetic images of CO isotopologues lines with different disk inclinations. By extracting the velocity perturbations from these images, we assess the observability of VSI-induced features using ALMA. Our main results can be summarized as follows:

1. The VSI perturbations exhibit stronger growth in a more thermally stratified disk, resulting in a higher level of turbulence at saturation. In terms of the Reynolds stress responsible for angular momentum transport to thermal pressure, $\alpha_{R\phi} = 1 \times 10^{-4}$ in the isothermal disk, which increases to 1×10^{-3} and 2×10^{-3} in the thermally stratified disks with $n = 2$ and 3 , respectively.
2. Synthetic observations of the turbulent disks induced by the VSI reveal distinct residual velocities. In isothermal disks, these velocities appear as quasi-axisymmetric rings, while in thermally stratified disks, they manifest as ring segments, once the Keplerian rotational velocity is subtracted. At an inclination angle of $i = 20^\circ$, the amplitude of the residual velocities amounts to $\sim 50, 80,$ and 100 m s^{-1} in the disks with $n = 1, 2,$ and 3 , respectively. These levels of the VSI signatures can potentially be observable by the ALMA despite their complex shapes induced by the non-monotonic vertical shear profile resulting from the thermal stratification as well as Kelvin-Helmholtz-like parasitic instability.
3. The enhancement of the radial and the azimuthal components of the VSI-driven velocity perturbations with increasing thermal stratification of the disk enables kinematic features, in the form of ring segments, to remain observable even at disk inclinations as high as $i = 45^\circ$. The magnitude of the observed velocity perturbations depends on the tracer used. While the effect of the optical depth is insignificant in the isothermal disk, in

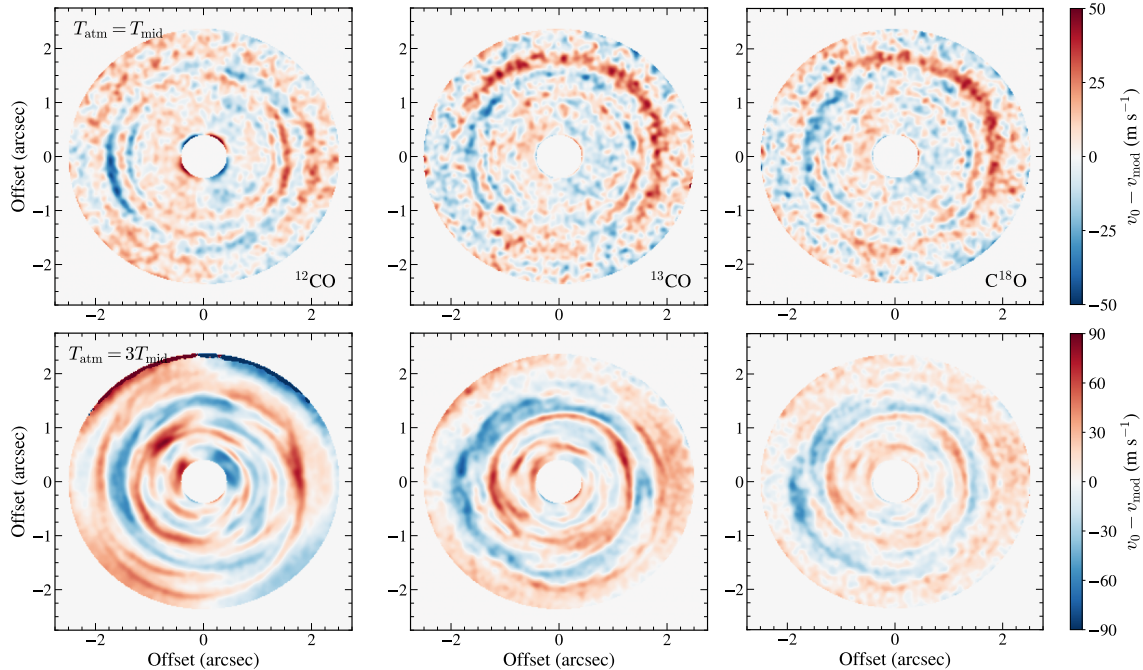


Figure 13. Velocity residual maps for ^{12}CO , ^{13}CO , and C^{18}O from left to right in the disks with $n = 1$ (top) and 3 (bottom) for an inclination of $i = 20^\circ$. In the isothermal disk, the magnitudes of the velocity residuals remain small, irrespective of the tracer elements. In the $n = 3$ disk, however, the velocity residual decreases as the tracers probe the regions closer to the midplane.

thermally stratified disks, the velocity perturbations decrease remarkably when transitioning from ^{12}CO to ^{13}CO to C^{18}O , as the latter probes closer to the midplane where vertical shear is weak.

ACKNOWLEDGMENTS

We are grateful to the referee for detailed and constructive comments. The work of H.-G.Y. was sup-

ported by the grants of Basic Science Research Program through the National Research Foundation of Korea (NRF) funded by the Ministry of Education (2022R1A6A3A13072598). The work of W.-T.K. was supported by a grant of the National Research Foundation of Korea (2022R1A2C1004810). JB acknowledges support from NASA XRP grant No. 80NSSC23K1312.

REFERENCES

- Bai, X.-N., & Stone, J. M. 2013, *ApJ*, 769, 76, doi: [10.1088/0004-637X/769/1/76](https://doi.org/10.1088/0004-637X/769/1/76)
- Balbus, S. A., & Hawley, J. F. 1991, *ApJ*, 376, 214, doi: [10.1086/170270](https://doi.org/10.1086/170270)
- Barker, A. J., & Latter, H. N. 2015, *MNRAS*, 450, 21, doi: [10.1093/mnras/stv640](https://doi.org/10.1093/mnras/stv640)
- Barraza-Alfaro, M., Flock, M., & Henning, T. 2024, *A&A*, 683, A16, doi: [10.1051/0004-6361/202347726](https://doi.org/10.1051/0004-6361/202347726)
- Barraza-Alfaro, M., Flock, M., Marino, S., & Pérez, S. 2021, *A&A*, 653, A113, doi: [10.1051/0004-6361/202140535](https://doi.org/10.1051/0004-6361/202140535)
- Benítez-Llambay, P., & Masset, F. S. 2016, *ApJS*, 223, 11, doi: [10.3847/0067-0049/223/1/11](https://doi.org/10.3847/0067-0049/223/1/11)
- Chiang, E. I., & Goldreich, P. 1997, *ApJ*, 490, 368, doi: [10.1086/304869](https://doi.org/10.1086/304869)
- Cui, C., & Bai, X.-N. 2020, *ApJ*, 891, 30, doi: [10.3847/1538-4357/ab7194](https://doi.org/10.3847/1538-4357/ab7194)
- D’Alessio, P., Cantö, J., Calvet, N., & Lizano, S. 1998, *ApJ*, 500, 411, doi: [10.1086/305702](https://doi.org/10.1086/305702)
- D’Alessio, P., Cantó, J., Hartmann, L., Calvet, N., & Lizano, S. 1999, *ApJ*, 511, 896, doi: [10.1086/306704](https://doi.org/10.1086/306704)
- Dartois, E., Dutrey, A., & Guilloteau, S. 2003, *A&A*, 399, 773, doi: [10.1051/0004-6361:20021638](https://doi.org/10.1051/0004-6361:20021638)
- de Val-Borro, M., Edgar, R. G., Artymowicz, P., et al. 2006, *MNRAS*, 370, 529, doi: [10.1111/j.1365-2966.2006.10488.x](https://doi.org/10.1111/j.1365-2966.2006.10488.x)
- Disk Dynamics Collaboration, Armitage, P. J., Bae, J., et al. 2020, arXiv e-prints, arXiv:2009.04345, doi: [10.48550/arXiv.2009.04345](https://doi.org/10.48550/arXiv.2009.04345)
- Dullemond, C. P., Juhasz, A., Pohl, A., et al. 2012, RADMC-3D: A multi-purpose radiative transfer tool, Astrophysics Source Code Library, record ascl:1202.015
- Dullemond, C. P., Birnstiel, T., Huang, J., et al. 2018, *ApJL*, 869, L46, doi: [10.3847/2041-8213/aaf742](https://doi.org/10.3847/2041-8213/aaf742)

- Facchini, S., Benisty, M., Bae, J., et al. 2020, *A&A*, 639, A121, doi: [10.1051/0004-6361/202038027](https://doi.org/10.1051/0004-6361/202038027)
- Flaherty, K., Hughes, A. M., Simon, J. B., et al. 2020, *ApJ*, 895, 109, doi: [10.3847/1538-4357/ab8cc5](https://doi.org/10.3847/1538-4357/ab8cc5)
- Flaherty, K. M., Hughes, A. M., Rosenfeld, K. A., et al. 2015, *ApJ*, 813, 99, doi: [10.1088/0004-637X/813/2/99](https://doi.org/10.1088/0004-637X/813/2/99)
- Flaherty, K. M., Hughes, A. M., Teague, R., et al. 2018, *ApJ*, 856, 117, doi: [10.3847/1538-4357/aab615](https://doi.org/10.3847/1538-4357/aab615)
- Flaherty, K. M., Hughes, A. M., Rose, S. C., et al. 2017, *ApJ*, 843, 150, doi: [10.3847/1538-4357/aa79f9](https://doi.org/10.3847/1538-4357/aa79f9)
- Flock, M., Nelson, R. P., Turner, N. J., et al. 2017, *ApJ*, 850, 131, doi: [10.3847/1538-4357/aa943f](https://doi.org/10.3847/1538-4357/aa943f)
- Flock, M., Turner, N. J., Nelson, R. P., et al. 2020, *ApJ*, 897, 155, doi: [10.3847/1538-4357/ab9641](https://doi.org/10.3847/1538-4357/ab9641)
- Flores-Rivera, L., Flock, M., & Nakatani, R. 2020, *A&A*, 644, A50, doi: [10.1051/0004-6361/202039294](https://doi.org/10.1051/0004-6361/202039294)
- Fricke, K. 1968, *ZA*, 68, 317
- Fukuhara, Y., Okuzumi, S., & Ono, T. 2023, *PASJ*, 75, 233, doi: [10.1093/pasj/psac107](https://doi.org/10.1093/pasj/psac107)
- Goldreich, P., & Schubert, G. 1967, *ApJ*, 150, 571, doi: [10.1086/149360](https://doi.org/10.1086/149360)
- Huang, P., Isella, A., Li, H., Li, S., & Ji, J. 2018, *ApJ*, 867, 3, doi: [10.3847/1538-4357/aae317](https://doi.org/10.3847/1538-4357/aae317)
- Latter, H. N., & Papaloizou, J. 2018, *MNRAS*, 474, 3110, doi: [10.1093/mnras/stx3031](https://doi.org/10.1093/mnras/stx3031)
- Law, C. J., Teague, R., Loomis, R. A., et al. 2021, *ApJS*, 257, 4, doi: [10.3847/1538-4365/ac1439](https://doi.org/10.3847/1538-4365/ac1439)
- Lesur, G., Kunz, M. W., & Fromang, S. 2014, *A&A*, 566, A56, doi: [10.1051/0004-6361/201423660](https://doi.org/10.1051/0004-6361/201423660)
- Lesur, G., Flock, M., Ercolano, B., et al. 2023, in *Astronomical Society of the Pacific Conference Series*, Vol. 534, *Protostars and Planets VII*, ed. S. Inutsuka, Y. Aikawa, T. Muto, K. Tomida, & M. Tamura, 465
- Lin, M.-K., & Youdin, A. N. 2015, *ApJ*, 811, 17, doi: [10.1088/0004-637X/811/1/17](https://doi.org/10.1088/0004-637X/811/1/17)
- Lynden-Bell, D., & Pringle, J. E. 1974, *MNRAS*, 168, 603, doi: [10.1093/mnras/168.3.603](https://doi.org/10.1093/mnras/168.3.603)
- Melon Fuksman, J. D., Flock, M., & Klahr, H. 2024, *A&A*, 682, A139, doi: [10.1051/0004-6361/202346554](https://doi.org/10.1051/0004-6361/202346554)
- Nelson, R. P., Gressel, O., & Umurhan, O. M. 2013, *MNRAS*, 435, 2610, doi: [10.1093/mnras/stt1475](https://doi.org/10.1093/mnras/stt1475)
- Perez, S., Dunhill, A., Casassus, S., et al. 2015, *ApJL*, 811, L5, doi: [10.1088/2041-8205/811/1/L5](https://doi.org/10.1088/2041-8205/811/1/L5)
- Pfeil, T., Birnstiel, T., & Klahr, H. 2023, *ApJ*, 959, 121, doi: [10.3847/1538-4357/ad00af](https://doi.org/10.3847/1538-4357/ad00af)
- Pinte, C., Teague, R., Flaherty, K., et al. 2023, in *Astronomical Society of the Pacific Conference Series*, Vol. 534, *Protostars and Planets VII*, ed. S. Inutsuka, Y. Aikawa, T. Muto, K. Tomida, & M. Tamura, 645, doi: [10.48550/arXiv.2203.09528](https://doi.org/10.48550/arXiv.2203.09528)
- Pinte, C., van der Plas, G., Ménard, F., et al. 2019, *Nature Astronomy*, 3, 1109, doi: [10.1038/s41550-019-0852-6](https://doi.org/10.1038/s41550-019-0852-6)
- Robert, C. M. T., Méheut, H., & Ménard, F. 2020, *A&A*, 641, A128, doi: [10.1051/0004-6361/201937414](https://doi.org/10.1051/0004-6361/201937414)
- Rosotti, G. P. 2023, *NewAR*, 96, 101674, doi: [10.1016/j.newar.2023.101674](https://doi.org/10.1016/j.newar.2023.101674)
- Rosotti, G. P., Tazzari, M., Booth, R. A., et al. 2019, *MNRAS*, 486, 4829, doi: [10.1093/mnras/stz1190](https://doi.org/10.1093/mnras/stz1190)
- Rosotti, G. P., Teague, R., Dullemond, C., Booth, R. A., & Clarke, C. J. 2020, *MNRAS*, 495, 173, doi: [10.1093/mnras/staa1170](https://doi.org/10.1093/mnras/staa1170)
- Schöier, F. L., van der Tak, F. F. S., van Dishoeck, E. F., & Black, J. H. 2005, *A&A*, 432, 369, doi: [10.1051/0004-6361:20041729](https://doi.org/10.1051/0004-6361:20041729)
- Shakura, N. I., & Sunyaev, R. A. 1973, *A&A*, 24, 337
- Simon, J. B., Bai, X.-N., Stone, J. M., Armitage, P. J., & Beckwith, K. 2013, *ApJ*, 764, 66, doi: [10.1088/0004-637X/764/1/66](https://doi.org/10.1088/0004-637X/764/1/66)
- Stoll, M. H. R., & Kley, W. 2014, *A&A*, 572, A77, doi: [10.1051/0004-6361/201424114](https://doi.org/10.1051/0004-6361/201424114)
- Stoll, M. H. R., Kley, W., & Picogna, G. 2017, *A&A*, 599, L6, doi: [10.1051/0004-6361/201630226](https://doi.org/10.1051/0004-6361/201630226)
- Svanberg, E., Cui, C., & Latter, H. N. 2022, *MNRAS*, 514, 4581, doi: [10.1093/mnras/stac1598](https://doi.org/10.1093/mnras/stac1598)
- Teague, R. 2019, *The Journal of Open Source Software*, 4, 1220, doi: [10.21105/joss.01220](https://doi.org/10.21105/joss.01220)
- Teague, R., & Foreman-Mackey, D. 2018, *bettermoments: A robust method to measure line centroids*, v1.0, Zenodo, doi: [10.5281/zenodo.1419754](https://doi.org/10.5281/zenodo.1419754)
- Teague, R., Guilloteau, S., Semenov, D., et al. 2016, *A&A*, 592, A49, doi: [10.1051/0004-6361/201628550](https://doi.org/10.1051/0004-6361/201628550)
- Teague, R., Henning, T., Guilloteau, S., et al. 2018, *ApJ*, 864, 133, doi: [10.3847/1538-4357/aad80e](https://doi.org/10.3847/1538-4357/aad80e)
- Teague, R., Bae, J., Aikawa, Y., et al. 2021, *ApJS*, 257, 18, doi: [10.3847/1538-4365/ac1438](https://doi.org/10.3847/1538-4365/ac1438)
- Trapman, L., Rosotti, G., Bosman, A. D., Hogerheijde, M. R., & van Dishoeck, E. F. 2020, *A&A*, 640, A5, doi: [10.1051/0004-6361/202037673](https://doi.org/10.1051/0004-6361/202037673)
- Urpin, V. 2003, *A&A*, 404, 397, doi: [10.1051/0004-6361:20030513](https://doi.org/10.1051/0004-6361:20030513)
- Urpin, V., & Brandenburg, A. 1998, *MNRAS*, 294, 399, doi: [10.1046/j.1365-8711.1998.01118.x](https://doi.org/10.1046/j.1365-8711.1998.01118.x)
- Wilson, T. L., & Rood, R. 1994, *ARA&A*, 32, 191, doi: [10.1146/annurev.aa.32.090194.001203](https://doi.org/10.1146/annurev.aa.32.090194.001203)
- Yun, H.-G., Kim, W.-T., & Bae, J. 2024, submitted
- Zhang, S., Zhu, Z., & Jiang, Y.-F. 2024, *ApJ*, 968, 29, doi: [10.3847/1538-4357/ad4109](https://doi.org/10.3847/1538-4357/ad4109)
- Ziampras, A., Kley, W., & Nelson, R. P. 2023, *A&A*, 670, A135, doi: [10.1051/0004-6361/202245325](https://doi.org/10.1051/0004-6361/202245325)

APPENDIX

A. TEST SIMULATIONS

In the appendix, we demonstrate the reliability of our numerical results by examining the effects of numerical resolution and boundary conditions on the models with $n = 1, 2$ and 3 . To assess convergence, we employ the ratio of volume-averaged Reynolds stress to thermal pressure as defined in Equation (6).

A.1. Resolution Test

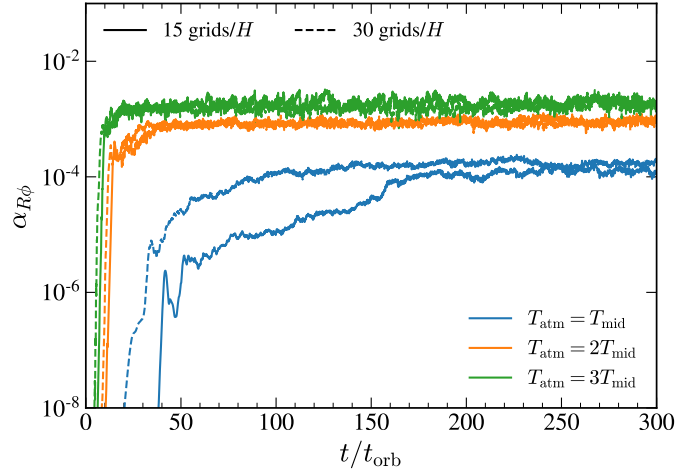


Figure 14. Comparison of $\alpha_{R\phi}$ between models with different resolutions. The solid and dashed lines represent the models with 15 and 30 cells per scale height, respectively. While $\alpha_{R\phi}$ varies with resolution at $t/t_{\text{orb}} \lesssim 250$ in the vertically isothermal disk, it shows almost no dependence on resolution in the thermally stratified disk. In both cases, the saturated value of $\alpha_{R\phi}$ remains essentially unaffected by resolution.

Flores-Rivera et al. (2020) recently argued accurately capturing the VSI in their 2.5D simulations requires resolving disks with more than 64 cells per scale height. Our 3D disk models presented in the main sections adopt a resolution of 15 cells per scale height, lower than the minimum suggested resolution by Flores-Rivera et al. (2020). To assess if our results are affected by this resolution, we conduct additional 3D simulations for models with $n = 1, 2$, and 3 , resolved by 30 cells per scale height.

Figure 14 compares the values of $\alpha_{R\phi}$ from the high-resolution runs with those from the standard runs. We find the temporal changes in $\alpha_{R\phi}$ depend on the resolution at $t/t_{\text{orb}} \lesssim 200$ in the $n = 1$ model. However, the difference is almost negligible in $n = 2$ and 3 models. Also, saturated values of $\alpha_{R\phi}$ are insensitive to resolution in all models. This confirms that our models with 15 cells per scale height produce reliable results in terms of saturated turbulence levels and the presence of quasi-axisymmetric structures in synthetic maps.

A.2. Boundary Condition Test

One characteristic feature of the VSI is the formation of vertically elongated structures (Nelson et al. 2013; Latter & Papaloizou 2018). As these structures typically develop near the disk surface in isothermal models, the boundary conditions at the meridional boundaries may potentially alter the outcomes of hydrodynamic simulations. The models outlined in the main sections utilize reflecting boundary conditions at the meridional boundaries. Here, we compare the results using reflecting and zero-gradient boundary conditions, the latter allowing gas to flow both inwards and outwards.

Figure 15 plots the resulting $\alpha_{R\phi}$ for the models with $n = 1, 2, 3$. In the isothermal disk, $\alpha_{R\phi}$ depend on the boundary conditions at $t/t_{\text{orb}} \lesssim 200$, eventually converging to a constant value $\alpha_{R\phi} \sim 10^{-4}$ at later times. In the thermally stratified disk, the effects of boundary conditions on turbulence levels are nearly negligible at almost all times. This

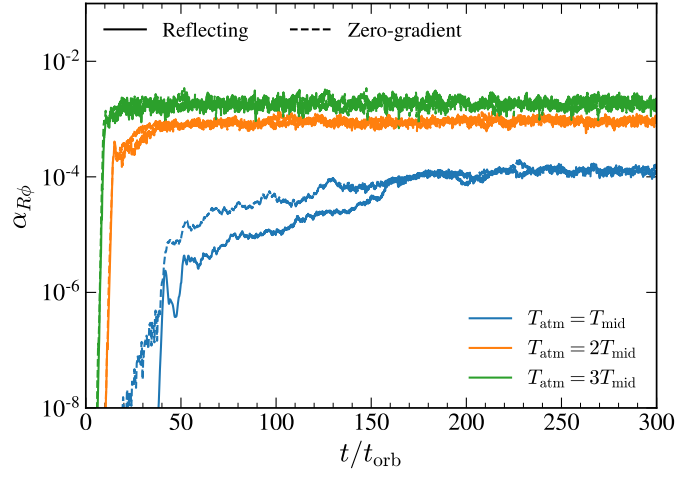


Figure 15. Comparison of $\alpha_{R\phi}$ from models with reflecting (*solid*) and zero-gradient (*dashed*) boundary conditions. Irrespective of vertical thermal stratification, saturated turbulence shows little sensitivity to the meridional boundary conditions at $t/t_{\text{orb}} \gtrsim 200$.

suggests that the turbulence induced by the VSI remains largely unaffected by the choice of boundary conditions. This validates our findings regarding the observability of the VSI in thermally stratified disks.